Light absorption enhancement and laser-induced damage ability improvement of AA 6061 with non-porous alumina /CdSe@Al_2O_3/SiO_2 functional gradient films

Jiaheng Yin, Lihua Lu, Yaowen Cui*, Yongzhi Cao and Yunlong Du

Center for Precision Engineering, Harbin Institute of Technology, Harbin150001, PR China

*Corresponding author

Yaowen Cui. Email: yaowen.xinxin.cui@outlook.com; Tel: +86-451-86412924; Fax: +86-451-86415244

Abstract: Numerical calculations of ultraviolet to near-infrared absorption spectra by cadmium selenide quantum dots (CdSe QDs) doped in anodic aluminum oxide pores were performed using a finite-difference time-domain model. The height, diameter, and periodic spacing of the pores were optimized. Light absorption by the dots was enhanced by increasing the height and decreasing the diameter of the pores. When the height was less than 1 μm, visible light absorption was enhanced as the spacing was reduced from 400 nm to 100 nm. No enhancement was observed for heights greater than 6 μm. Finally, the optical mode coupling of the aluminum oxide and the quantum dots was enhanced by decreasing the pore diameter and periodic spacing, and increasing the height. Laser ablation verified light absorption enhancement by the CdSe QDs. The experiment verified the improvement of the laser-induced damage ability with wavelength of 355-nm after aluminum alloy 6061 coated with functional films, which was fabricated based on numerical calculations.

Keywords: CdSe QDs, AA 6061, light absorption, laser ablation

1. Introduction

With the gradual scarcity of traditional fossil fuel resources such as coal, oil, and natural gas, coupled with the fact that they will cause serious environmental pollution and the greenhouse effect, finding new energy sources to replace traditional fossil fuels has become a major issue for contemporary technology to solve. Among them, the fusion energy produced by laser-driven controlled inertial confinement fusion (ICF) is valued by all countries for its rich fuel, clean materials, and safety of fusion reactors [1]. Representative examples include the large-scale laser tritium-deuterium fusion device built at Lawrence Livermore National Laboratory (LLNL) initiated by the U.S. Department of Energy in 1995-the "National Ignition Facility" (NIF) [2-4]. The new

 doi:10.20944/preprints202201.0169.v1

milestone now reached in August 2021 is an energy yield from the target of more than 1.3 MJ, representing around 70 percent of the energy that the laser pulse had delivered to the fuel capsule in its sights, and "generating more than 10 quadrillion watts of fusion power for 100 trillionths of a second," according to NIF[5]. French Atomic Energy and Alternative Energy Commission approved the "Laser Megajoule, LMJ" plan, The Rutherford-Alpton Laboratory of the Committee for Scientific and Technical Equipment of the United Kingdom used the Perwatt laser for the first time in the world, and Japan built the first Perwatt laser in Asia as the GEKKO-XII high-energy nanosecond at the Laser Engineering Institute of Osaka University. As part of the facility, Russia's PEARL-X is a next-generation Perwatt laser facility, etc. China's ultra-high-power laser facility at the Shanghai Institute of Optics and Mechanics also has world-leading equipment [6].

Aluminum alloy is used as the terminal optical component bracket due to its excellent mechanical properties. If the stray light, ghost image, etc. are improperly handled, or due to the effect of the beam transmission system diaphragm, the laser would irradiate the surface of aluminum alloy and cause its damage happen [7, 8]. In addition, the splashed metal particles may adhere to the surface of the optical element, causing secondary pollution on the surface of the optical element, and reducing the laser-induced damage threshold (LIDT) of the optical element by about 60% [9-12]. Although we can continuously improve the processing and manufacturing accuracy of optical components, the influence of system stray light on the aluminum alloy "framework" is inevitable. Therefore, to alleviate the damage of optical components, stray light absorption management must be studied. While ensuring the processing quality of optical components, the study of laser-induced damage mechanism and damage protection of aluminum alloy frames is also a key technical issue that cannot be ignored.

A key technical issue is the absorption of stay light [13] in nuclear energy system. Aluminum alloy frames normally require surface treatment to eliminate stray reflections. Zhu *et al.* [14] fabricated a broadband plasmonic absorber with an average absorbance of ≈99% from 400 nm to 10 μm through assembly of Au nanoparticles onto nano-porous template. In addition, Zhang *et al.* designed and illustrated an ultrathin Ag nanocomposite absorber with Ag nanocomposites could eliminate over 90% stray light from 400-600 nm wavelength. But the complicated and time-

Preprints (www.preprints.org) | NOT PEER-REVIEWED | Posted: 12 January 2022 doi:10.20944/preprints202201.0169.v1

consuming fabrication technology combined with noble metals such as Au and Ag restrict the application in aluminum alloy frame. This requires light absorbing materials in the pores of anodic aluminum oxide (AAO). CdSe quantum dots (QDs) have been used to absorb light with relatively low cost [15, 16]. Recently, Kohnehpoushi *et al.*[15] described visible light absorption enhancement in a CdSe-QD-sensitized TiO_2 periodic nanorod array. The enhancement mechanism was related to the diameter, height, and periodic spacing of the TiO_2 nanorods.

Here, we examined light absorption enhancement in AAO nanopores after incorporation of CdSe QDs (See in Figure 1). The use of CdSe QDs in AAO pores, rather than in semiconductors such as TiO_2, ZnO, or Si, was because they can be used to eliminating stray light in ICF systems. Two-dimensional finite-difference time-domain (FDTD) calculations were used to solve Maxwell's equations. The QD diameters were 10 nm and the grid size in the X- and Y-directions was 1 nm, while that in Z-direction was 10^{-4} nm. Periodic boundary conditions were applied in the X-direction and perfectly matched boundary-layer conditions were used in the Y-direction. Ultraviolet (UV) to near-infrared light (200–1000 nm) in the p-polarization plane was incident in the forward Y-direction. In the FDTD simulations, each electric field component (Ex, Ey, Ez) was calculated at a different location within a Yee cell to determine the absorption profile, as given by equation (1) as follows.

$$P_{abs} = -0.5\omega |\mathbf{E}|^2 \operatorname{Im}(\varepsilon_\omega) \quad (1)$$

Where P_{abs} is the power absorbed per unit volume at each position, ω is the angular frequency, $\mathbf{E}$ is the total electric field amplitude, and ε_ω is the permittivity of the material. They are generated by laser irradiation calculated by particle counter which firstly used to judge the LIDT of materials. Nd: YAG laser is used to irradiate the material. The ablation craters are detected by scanning electron microscopy (SEM).

Preprints (www.preprints.org) | NOT PEER-REVIEWED | Posted: 12 January 2022 doi:10.20944/preprints202201.0169.v1

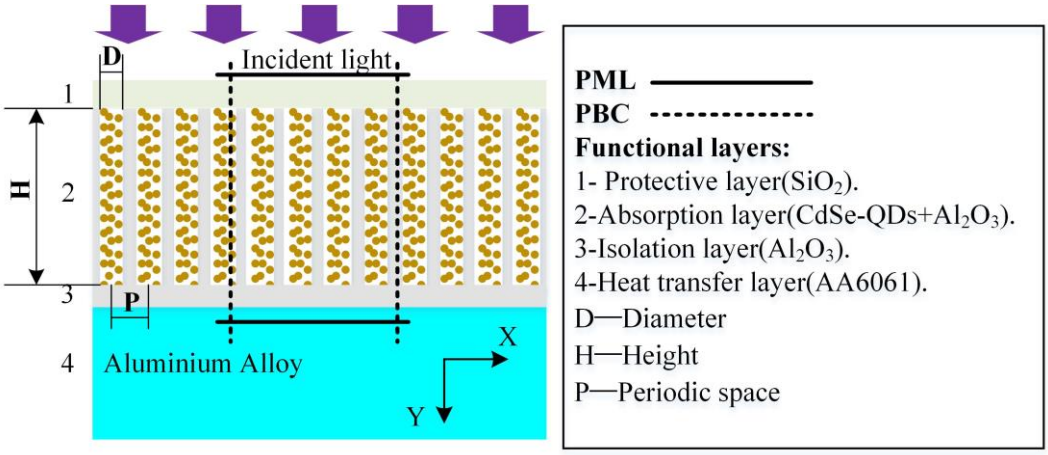

Fig. 1. Schematic of simulated anodic aluminum oxide nanopores with embedded CdSe quantum dots.

2. Theories and simulation

Semiconductor nanocrystals (SNCs) like cadmium selenide (CdSe) quantum dots offer widely application in the field of photovoltaics, solar energy harvesting, nanophotonics, imaging, sensing and other fields [17-22]. Since incident radiation excitation of free electrons, metal nanoparticles (MNPs) can generate intense electric fields in their vicinity [23]. When SNCs are held in close vicinity of MNPs, the high electric fields induced by MNPs can lead to enhanced absorption in SNCs. This absorption phenomena in both nanostructures (MNPs and SNCs) are described by various theories. Plasmons's originates from collective oscillations of free conduction electrons [24] while excitation is a bound state of electron–hole pair [25], which makes the modeling of these hybrid hetero-structures very difficult owing to accurately describe the characteristics of the system, we need to effectively combine two different theories. The models which has been used practically describe hetero-structure systems were complex. People regard nanostructures as independent units (applicable for weak coupling regime) with independent dielectric functions which could be taking classical electro-dynamic interactions within finite-difference time-domain (FDTD) or discrete dipole approximation (DDA) [26, 27].

The numerical study of proposed functional films was conducted by using commercial-grade simulator based on the FDTD method [28]. Here the nanostructures films was set as three functional films (nonporous alumina isolating film, a CdSe@Al_2O_3 nano-composites absorption film, and a SiO_2 dielectric sealing protective film). Figure 1 shows the simulated unit cell of the periodic model.

Preprints (www.preprints.org) | NOT PEER-REVIEWED | Posted: 12 January 2022 doi:10.20944/preprints202201.0169.v1

In the simulation procedure, height of the Al_2O_3 ellipsoids were 8 μm, 6 μm, 4 μm and 2 μm. The diameters of nanopores were 60 nm, 70 nm, 80 nm and 100 nm with the periodic space of 100 nm, 200 nm, 300 nm and 400 nm. Over the top layer, Ultraviolet (UV) to near infrared (200–1000 nm) in the p-polarization plane was incident in the forward direction of the y-axis. Finally, the specific absorption is calculated using equation (2) and (3). The dielectric function of materials used in the simulation was fitted with the experimental data to ensure that simulated results agree with measured ones.

$$T_\lambda = \frac{\frac{1}{2}\int \mathrm{real}(\mathbf{P}(\lambda)^{\mathrm{monitor}}) \cdot d\mathbf{S}}{\mathrm{sourcepower}} \quad (2)$$

$$A_\lambda = 1 - T(\lambda) - R(\lambda) \quad (3)$$

Figure 2 plots the absorption spectra of AAO pores with embedded QDs for various height-to-diameter aspect ratios and periodic space. In Fig. 2(a), the light absorption was enhanced for wavelengths less than 550 nm with increasing pore height and decreasing diameter. In the infrared region, decreased height and diameter enhanced light absorption. This was consistent with light absorption as a function of periodic pore spacing over the range 200–400 nm [Fig. 2(b–d)]. The results for 200-nm and 300-nm space were close, the light absorption sharply decreased for a 400-nm spacing. Fig. 4(a–d) revealed shifts in the absorption peak in the 300–500 nm range toward lower wavelengths with increasing pore spacing. This indicated an increase in the AAO bandgap. The enhanced light absorption was largely related to the height of the pores. Thus, in the following, the heights of pores embedded with QDs were increased to optimize absorption.

Preprints (www.preprints.org) | NOT PEER-REVIEWED | Posted: 12 January 2022 doi:10.20944/preprints202201.0169.v1

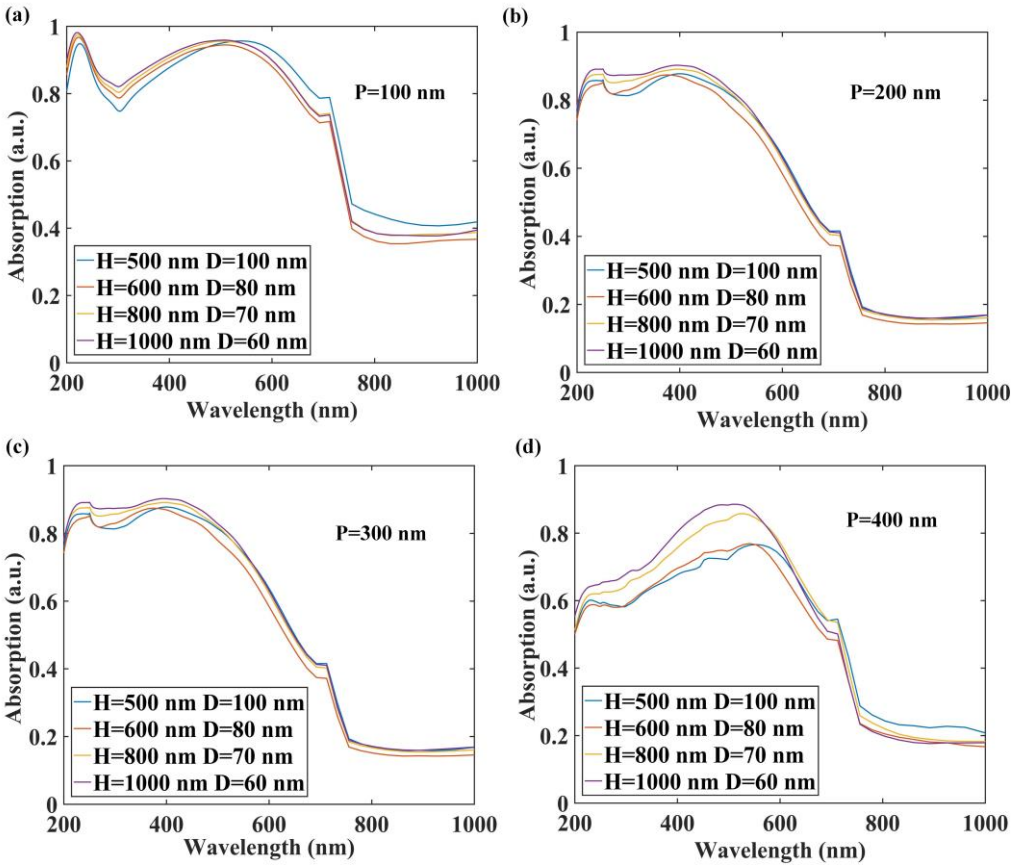

Figure 2 Light absorption enhancement in anodic aluminum oxide pores with embedded CdSe quantum dots at periodic space of (a) P=100 nm, (b) P=200 nm, (c) P=300 nm, and (d) P=400 nm.

Figure 3 plots the light absorption enhancement in AAO pores with embedded QDs for 100-nm, 200-nm, 300-nm, and 400-nm space. To optimize the spacing and height, the pore diameter-to-height ratios were 60:8000, 70: 6000, 80:4000, and 100: 2000. In Fig. 3(a–d), visible light absorption was enhanced with increasing spacing over the range 100–300 nm. However, when the spacing was 400 nm, the light absorption began to decrease. In the infrared region, the absorption enhancement at the 100-nm spacing was far greater than the other space. When the diameter-to-height ratios were 60:8000 and 70: 6000, the enhancement of the 100-nm spacing was more than 95% [Fig. 3(a,b)]. When the height was 2000 nm, the enhancement was about 90%, while those for other space were less than 60%. In the UV band, the absorption enhancement increased with increasing height and decreasing diameter. However, in Fig. 3(a), the enhancement was not apparent at heights over the range 6–8 μm.

Preprints (www.preprints.org) | NOT PEER-REVIEWED | Posted: 12 January 2022 doi:10.20944/preprints202201.0169.v1

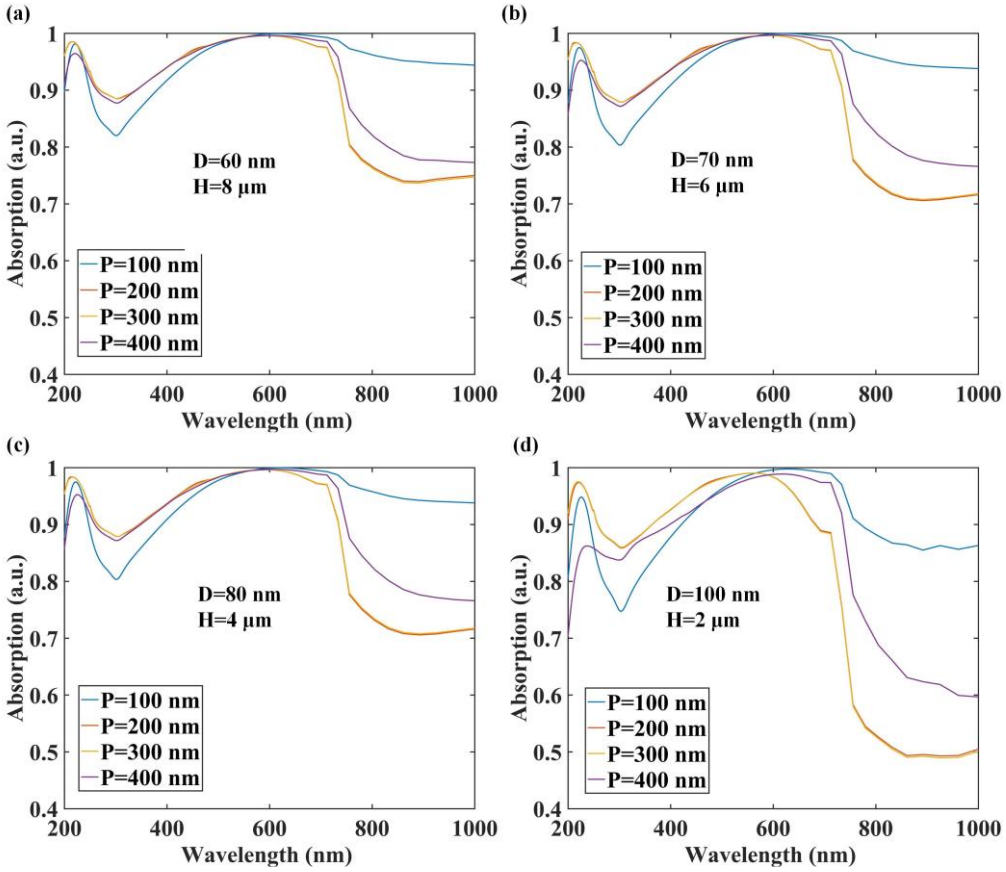

Fig. 3. Light absorption enhancement in anodic aluminum oxide pores with embedded CdSe quantum dots and 100-nm, 200-nm, 300-nm, and 400-nm periodic space for (a) D = 60 nm and H = 8 μm, (b) D = 70 nm and H = 6 μm, (c) D = 80 nm and H = 4 μm, and (d) D = 100 nm and H = 2 μm

3. Results and discussion

To verify the accuracy of the simulations and to demonstrate that the surface treatment of the aluminum alloy 6061 (AA 6061) increases light absorption, spectra were acquired before and after surface treatment. The height of the absorption layer was about 8 μm and the pore diameters were about 60 nm. The part of cross section of functional films shown in Fig. 4(a). Figure 4(b)-(f) demonstrate the distribution of elements of functional films. A Nd:YAG laser operating at 355 nm was used (Schematics of laser ablation testing equipment shown in Fig. S1). Laser ablation defects were detected with scanning electron microscopy, and a particle counter was used to record the number of particles created with various diameters. The experimental results in Figs. 4 and 5 indicate that regardless of the surface quality or the generated particles following surface anodizing, the AAO pores with embedded QDs exhibited higher light absorption than did undoped AA 6061. In most cases, more absorption indicated greater damage. However, the absorbed light was diffused

Preprints (www.preprints.org) | NOT PEER-REVIEWED | Posted: 12 January 2022 doi:10.20944/preprints202201.0169.v1

in deeper regions and the SiO_2 acted as a protective layer for the AA 6061 substrate. The melting and vaporization points of AAO are 2327 K and 3253 K, respectively. Those for SiO_2 are 2273 K and 2973 K, and those for AA 6061 are 923 K and 2740 K, respectively. These differences indicated that the protective effects were better than the absorptive effects. Hence, the functional layers absorbed more and experienced less damage, because of the AAO pores embedded with QDs. The QDs thus absorbed the light, and the higher absorption values of the AAO and the SiO_2 films provided the AA 6061 with greater protection against laser-induced damage.

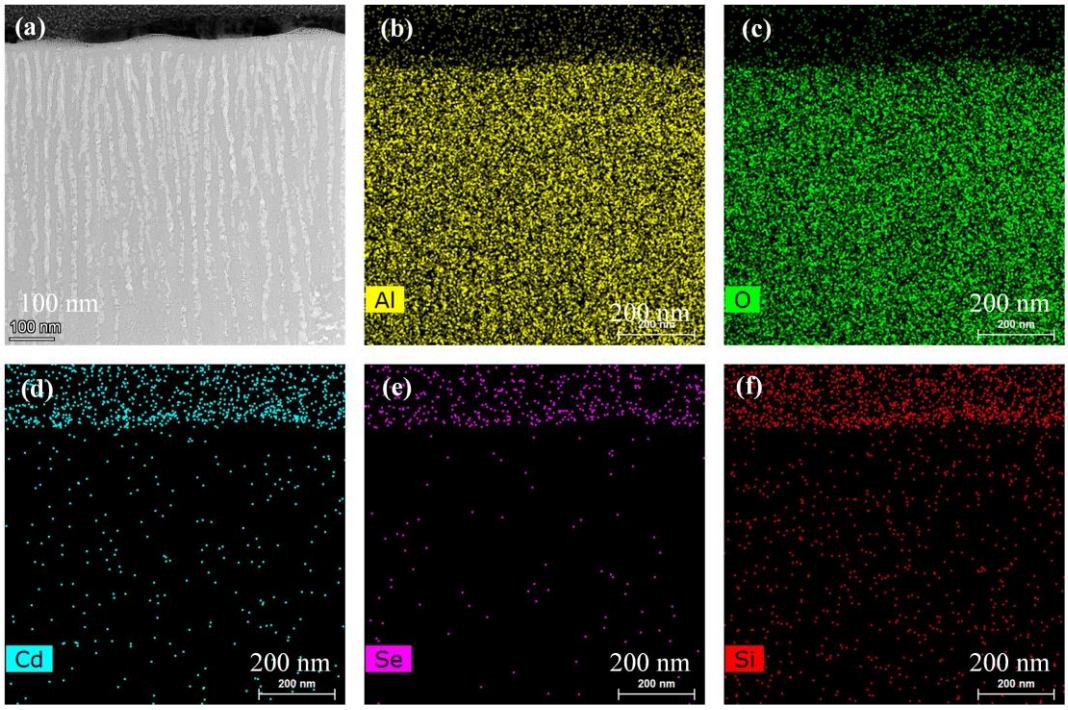

Fig.4 (a) Cross section of functional layers. (b) Distribution of aluminum of functional layers. (c) Distribution of oxygen elements of functional layers. (d) Distribution of cadmium of functional layers. (e) Distribution of selenium of functional layers. (f) Distribution of silicon of functional layers.

Figure 5 shows the surface morphology of AA 6061 after 15-time laser pulses with a 480-μm spot radius. In Fig. 5(a), AA 6061 coated with nonporous alumina isolating layer, a $CdSe@Al_2O_3$ nanocomposites absorption layer, and a SiO_2 dielectric sealing protective layer, the radius of the heat zone was less than 100 μm, and there was a cluster of ablation pits after solidification. The ablation zone cannot been seen, which was significantly less than the 0.7-mm^2 laser spot size (The enlarged view of ablation area is shown in Fig. 5(b)). This indicated that the surface treatment with functional layers absorbed light and protected the AA 6061 substrate. However, Figure 5 (c) shows

Preprints (www.preprints.org) | NOT PEER-REVIEWED | Posted: 12 January 2022 doi:10.20944/preprints202201.0169.v1

the morphology after being exposed to 15-time pulses of laser radiation of AA 6061 (The enlarged view of ablation area is shown in Fig. 5(d)). The areas of the heat zones were greater than 0.5 mm^2, which indicated damage at the edge of the Gaussian laser spot at a low power density. The enlarged figure in the upper right corner depicts the loose-layered structure after cooling for several days. It was in an unstable state that could peel away. To further verify that the AAO pores with embedded QDs absorbed the light, we used a particle counter to record the number of particles with various diameters created by the laser irradiation. The greater light absorption indicated stronger protection of the upper layer membrane and less particle contamination.

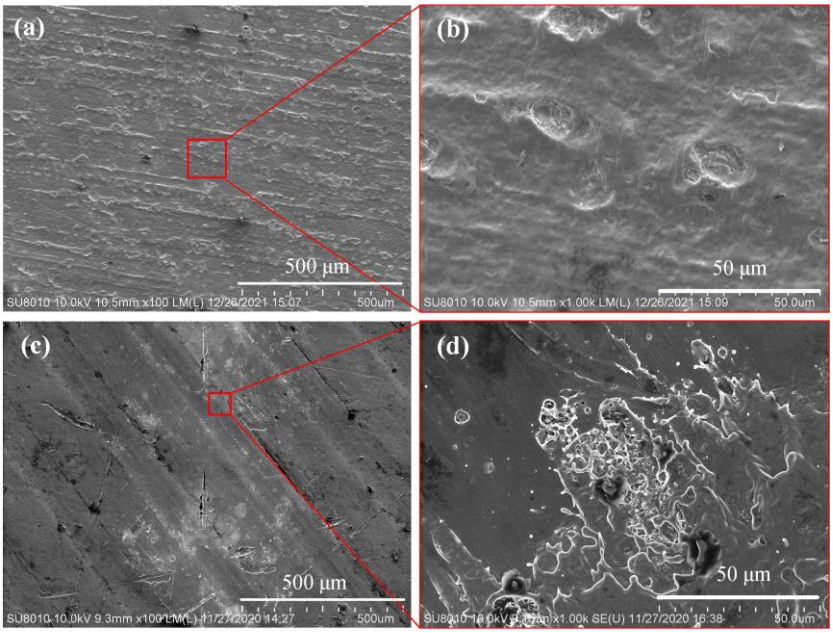

Fig. 5. 355-nm Nd:YAG laser irradiation of aluminum alloy 6061 at a fluence of 0.5 J/cm2 for laser irradiation times of 15. (a) With functional layers. (b) The enlarged view of ablation area of Fig. 4(a). (c) Without functional layers. (d) The enlarged view of ablation area of Fig. 4(c)

Figure 6 shows particles generated by fifteen pulses of laser irradiation (The specific number of particles is shown in Table 1 and Table 2 of Supplementary Materials). The particle numbers and their diameters were recorded after each laser shot. The total number of particles of AAO pores with embedded QDs were 1239. 57.6% of the 0.3-μm-diameter particles were produced during the first three laser pulses, and nearly 70 % of the rest were generated [Fig. 6(a)]. However, 31300 particles were generated when the AA 6061 surface was not treated with AAO pores with embedded QDs.

Preprints (www.preprints.org) | NOT PEER-REVIEWED | Posted: 12 January 2022 doi:10.20944/preprints202201.0169.v1

More than 90 % of the various particles diameters were produced during the first three laser pulses. This indicated that, without treatment, the surface could be easily damaged by laser irradiation. There were 101 particles with diameters of 5 μm. These could significantly contaminate an ICF system and affect optical transmission [Fig.6 (b)].

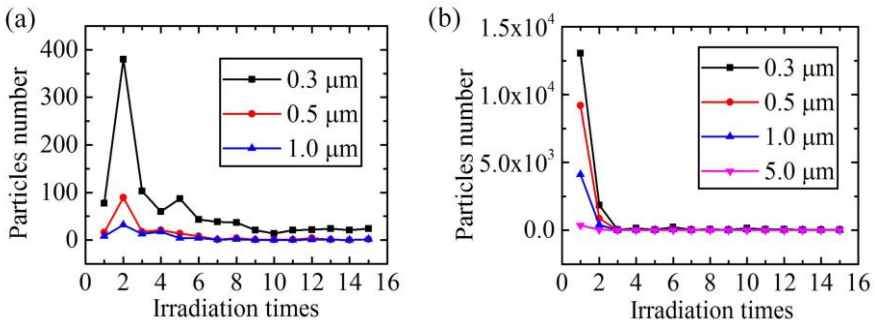

Fig. 6. Number and diameters of particles produced by a laser fluence of 0.5 J/cm2. (a) With functional layers. (b) Without functional layers.

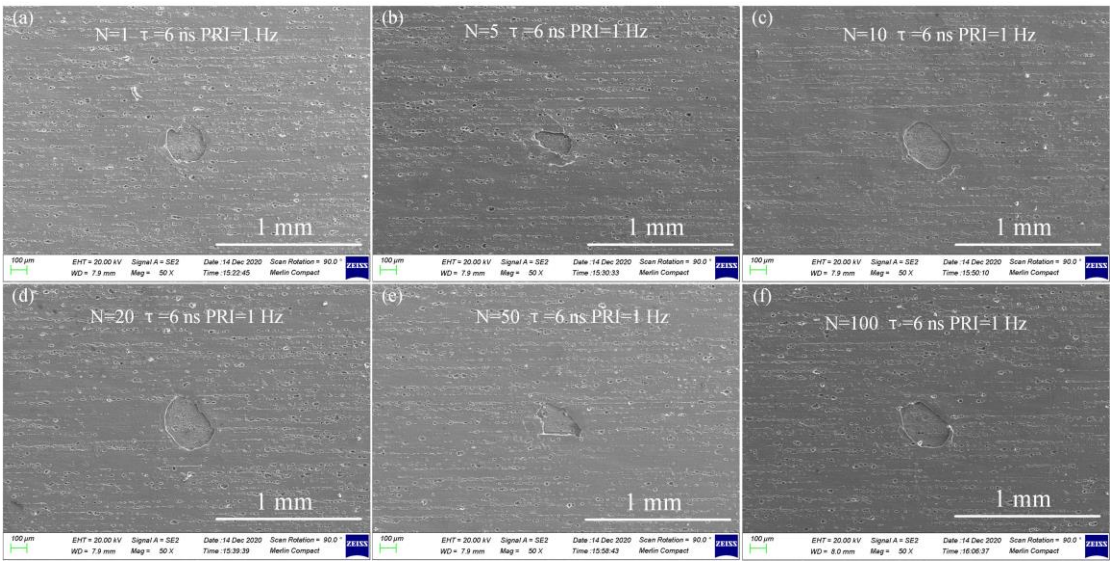

Fig. 7. 1064-nm Nd:YAG laser irradiation of aluminum alloy 6061 with functional layers at a fluence of 0.5 J/cm2 at (a)1 time, (b) 5 time, (c) 10 time, (d) 20 time, (e) 50 time, (f) 100 time irradiation.

Figure 7 demonstrates the morphologies of AA 6061 coated by AAO pores with embedded CdSe QDs and SiO_2 composite films at 1064 nm/0.5 J/cm^2 laser irradiation for (a) 1 time, (b) 5-time, (c) 10-time, (d) 20-time, (e) 50-time, (f) 100-time, respectively. Compared the morphologies of AA 6061 with functional films at a wavelength of 355-nm, the ablation areas and depths are more

Preprints (www.preprints.org) | NOT PEER-REVIEWED | Posted: 12 January 2022 doi:10.20944/preprints202201.0169.v1

obvious. According to simulation results, the light absorption of 355-nm is about 90 %, which is far more than that of 1064-nm wavelength (Morphologies of 355-nm laser irradiation were seen in Fig. S2). The energy levels of molecules mainly include the energy levels of electrons, the vibrational energy levels corresponding to the relative motion of atomic nuclei in molecules, and the rotational energy levels corresponding to the overall rotation of molecules. The interval between the vibrational energy level and the rotational energy level of most material molecules is the energy corresponding to the infrared photon. Therefore, when most substances are bathed in infrared light, material molecules can absorb a large number of infrared photons and transition to a high-energy level with faster vibration or rotation. The acceleration of molecular vibration or rotation in the micro corresponds to the temperature rise of the macro object - being heated. The energy of ultraviolet photons mostly corresponds to the energy level of electrons in the molecules mentioned above. However, UV laser can often make electrons transition from one atom to another, so as to change the structure of the whole molecule, that is, photochemical ablation.

4. Conclusion

In conclusion, enhanced light absorption in AAO pores with embedded CdSe QDs was investigated using FDTD-based simulations. Visible light absorption increased when the pore height was increased and the diameter was decreased. It was not enhanced when the height was greater than 8 μm. The absorption edge shifted toward UV wavelengths, which indicated an increased equivalent bandgap for the AAO pores with embedded QDs. In the near-infrared region, a large periodic spacing (p=400 nm) would absorb much more light for increased heights, relative to that observed for the 100-nm, 200-nm, and 300-nm space. Finally, experiments indicated that AAO pores with embedded QDs improved AA 6061 resistance to laser-induced damage with wavelength of 355 nm. The damage zone and ejected particles were much less pronounced than for untreated materials. The simulations agreed well with the experimental results and demonstrated that anodic aluminum oxide pores with embedded CdSe QDs enhanced the light absorption of AA 6061. Finally, the non-porous alumina /CdSe@Al_2O_3/SiO_2 functional gradient films can effectively absorb 355nm-UV stray light and improve the anti-laser-induced ability of AA 6061.

Acknowledgments

This work was supported by the National key Research and Development Program of China (No. 2017YFA0701200), the Fundamental Research Funds for the Central Universities (Grant No. HIT.OCEF. 2021002).

Reference

[1] W. Ganchang, The prospect of main energy sources in 21 century, Chinese Journal of Nuclear Science and Engineering 18 (1998) 97-108.
[2] L.F. Berzak Hopkins, L. Divol, A. Pak, E.L. Dewald, S. Bhandarkar, L.R. Bennedetti, T. Bunn, J. Biener, J. Crippen, D. Casey, D. Edgell, D.N. Fittinghoff, M. Gatu-Johnson, C. Goyon, S. Haan, R. Hatarik, M. Havre, D.D.-M. Ho, N. Izumi, J. Jaquez, S.F. Khan, G.A. Kyrala, T. Ma, A.J. Mackinnon, A.G. MacPhee, B.J. MacGowan, N.B. Meezan, J. Milovich, M. Millot, P. Michel, S.R. Nagel, A. Nikroo, P. Patel, J. Ralph, J.S. Ross, N.G. Rice, D. Strozzi, M. Stadermann, P. Volegov, C. Yeamans, C. Weber, C. Wild, D. Callahan, O.A. Hurricane, S. Le Pape, Fusion Energy Output Greater than the Kinetic Energy of an Imploding Shell at the National Ignition Facility, Physical Review Letters 120 (2018) 245003.245001-245003.245006.
[3] R. Betti, O.A. Hurricane, Inertial-Confinement fusion with lasers, Nature Physics 12 (2016) 435-448.
[4] M.J. Edwards, P.K. Patel, J.D. Lindl, L.J. Atherton, A. Zylstra, Progress towards ignition on the National Ignition Facility, Physics of Plasmas 20 (2013) 051003.
[5] NIF takes further stride towards fusion ignition, 2021.
[6] C.N. Danson, C. Haefner, J. Bromage, T. Butcher, J.C. Fchanteloup, E.A. Chowdhury, A. Galvanauskas, L.A. Gizzi, J. Hein, D.I. Hillier, Petawatt and exawatt class lasers worldwide, High Power Laser Science and Engineering (2019).
[7] J. Yin, Y. Cao, Y. Cui, L. Lu, J. Chen, Nd: YAG laser ablation of aluminum alloy 6061 before and after silicon dioxide coating, Journal of Alloys and Compounds 877 (2021) 160329.
[8] J. Gao, Y. Cao, L. Lu, Z. Hu, K. Wang, F. Guo, Y. Yan, Study on the interaction between nanosecond laser and 6061 aluminum alloy considering temperature dependence, Journal of Alloys and Compounds 892 (2022) 162044.
[9] F.Y. Genin, M.R. Kozlowski, M. Feit, Contamination effects on optical damage, Office of Scientific & Technical Information Technical Reports (1998).
[10] F.Y. Genin, K. Michlitsch, J. Furr, M.R. Kozlowski, P.A. Krulevitch, Laser-induced damage of fused silica at 355 and 1064 nm initiated at aluminum contamination particles on the surface, Laser-induced Damage in Optical Materials, 1997.
[11] A. Pereira, J.G. Coutard, S. Becker, I. Tovena, P. Bouchut, G. Ravel, Impact of organic contamination on 1064-nm laser-induced damage threshold of dielectric mirrors, International Society for Optics and Photonics (2006).
[12] K.J. Michlitsch, Laser-induced damage initiated on the surface of particle contamination fused silica at 1064nm, United States, 1998, pp. Medium: ED; Size: 51 p.; Other: FDE: PDF; PL:.
[13] J. Yin, Y. Cao, Research of laser-induced damage of aluminum alloy 5083 on micro-arc oxidation and composite coatings treatment, Optics Express 27 (2019) 18232-18245.

[14] L. Zhou, Y. Tan, D. Ji, B. Zhu, P. Zhang, J. Xu, Q. Gan, Z. Yu, J. Zhu, Self-assembly of highly efficient, broadband plasmonic absorbers for solar steam generation, Science advances 2 (2016) e1501227-e1501227.
[15] Saman, Kohnehpoushi, Mehdi, Eskandari, Bahram, Abdollahi, Nejand, Vahid, Ahmadi, Numerical calculation of visible light absorption enhancement of CdSe-quantum dot-sensitized TiO2 nanorod periodic array as photoanode, Journal of Physics D Applied Physics (2017).
[16] C. Ma, D. Wu, X. Yao, X. Liu, M. Wei, Y. Liu, Z. Ma, P. Huo, Y. Yan, Enhanced visible-light photocatalytic decomposition of organic dye over CdSe/Al2TiO5 heterojunction photocatalysts, Journal of Alloys and Compounds 712 (2017) 486-493.
[17] Y. Fu, H. Zhu, J. Chen, M.P. Hautzinger, X.Y. Zhu, S. Jin, Metal halide perovskite nanostructures for optoelectronic applications and the study of physical properties, Nature Reviews Materials 4 (2019) 169-188.
[18] D. Bimberg, Semiconductor nanostructures for flying q-bits and green photonics, Nanophotonics 7 (2018) 1245-1257.
[19] G. Xu, S. Zeng, B. Zhang, M.T. Swihart, K.-T. Yong, P.N. Prasad, New Generation Cadmium-Free Quantum Dots for Biophotonics and Nanomedicine, Chemical reviews 116 (2016) 12234-12327.
[20] L. Pulgar-Velásquez, J. Sierra-Ortega, J.A. Vinasco, D. Laroze, A. Radu, E. Kasapoglu, R.L. Restrepo, J.A. Gil-Corrales, A.L. Morales, C.A. Duque, Shallow Donor Impurity States with Excitonic Contribution in GaAs/AlGaAs and CdTe/CdSe Truncated Conical Quantum Dots under Applied Magnetic Field, Nanomaterials 11 (2021) 2832.
[21] E. Kolesova, A. Bulgakova, V. Maslov, A. Veniaminov, A. Dubavik, Y. Gun'ko, O. Efremenkova, V. Oleinikov, A. Orlova, Bactericidal Activity of Multilayered Hybrid Structures Comprising Titania Nanoparticles and CdSe Quantum Dots under Visible Light, Nanomaterials 11 (2021) 3331.
[22] F. Zhao, S. Hu, C. Xu, H. Xiao, X. Zhou, X. Zu, S. Peng, Effect of Copper Doping on Electronic Structure and Optical Absorption of Cd33Se33 Quantum Dots, Nanomaterials 11 (2021) 2531.
[23] G.V. Hartland, Optical Studies of Dynamics in Noble Metal Nanostructures, Chemical reviews 111 (2011) 3858-3887.
[24] D. Pines, D. Bohm, A Collective Description of Electron Interactions: II. Collective vs Individual Particle Aspects of the Interactions, Physical Review 85 (1952) 338-353.
[25] W.Y. Liang, Excitons, Physics Education 5 (1970) 226-228.
[26] V. Myroshnychenko, J. Rodríguez-Fernández, I. Pastoriza-Santos, A.M. Funston, C. Novo, P. Mulvaney, L.M. Liz-Marzán, F.J. García de Abajo, Modelling the optical response of gold nanoparticles, Chemical Society Reviews 37 (2008) 1792-1805.
[27] J. Zhao, A.O. Pinchuk, J.M. McMahon, S. Li, L.K. Ausman, A.L. Atkinson, G.C. Schatz, Methods for Describing the Electromagnetic Properties of Silver and Gold Nanoparticles, Accounts of Chemical Research 41 (2008) 1710-1720.
[28] Lumerical Solutions, Inc., http://www.lumerical.com/tcad-products/fdtd/, 2016.

Preprints (www.preprints.org) | NOT PEER-REVIEWED | Posted: 12 January 2022 doi:10.20944/preprints202201.0169.v1

Appendix. Supplementary material

Table S1 Particles generated by different laser irradiation times with laser fluence of 0.5 J/cm^2 of AA 6061 without functional layers

S. no	Diameters of particles (μm)				
	0.3	0.5	1.0	5.0	10.0
1	2141	572	199	3	0
2	10618	4142	1127	25	1
3	1112	252	52	0	0
4	5638	1807	504	6	0
5	1957	538	206	5	0
6	789	144	30	0	0
7	2296	561	145	2	0
8	2514	689	193	9	1
9	2179	459	116	5	0
10	1090	215	62	2	0
11	488	86	13	0	0
12	725	115	18	0	0
13	451	58	5	0	0
14	802	115	20	1	0
15	2182	495	156	9	0

Table S2 Particles generated by different laser irradiation times with laser fluence of 0.5 J/cm^2 with functional layers

S. no	Diameters of particles (μm)		
	0.3	0.5	1.0
1	77	16	8
2	380	89	32
3	103	18	13
4	60	21	18
5	87	14	4
6	43	8	4
7	38	1	1
8	37	4	2
9	20	1	0
10	14	1	0
11	21	1	0
12	22	4	1
13	24	1	1
14	21	0	0

Preprints (www.preprints.org) | NOT PEER-REVIEWED | Posted: 12 January 2022 doi:10.20944/preprints202201.0169.v1

15	24	2	2

The experimental system consists of a single longitudinal mode SAGA-S laser Nd: YAG laser, collimated light source, focusing lens, attenuator, aperture, an EPM2000 energy calorimeter, a sample carrier (two-dimensional adjustable, step-by-step accuracy is 10 um), an optical microscope and a computer. The experimental setup is depicted below.

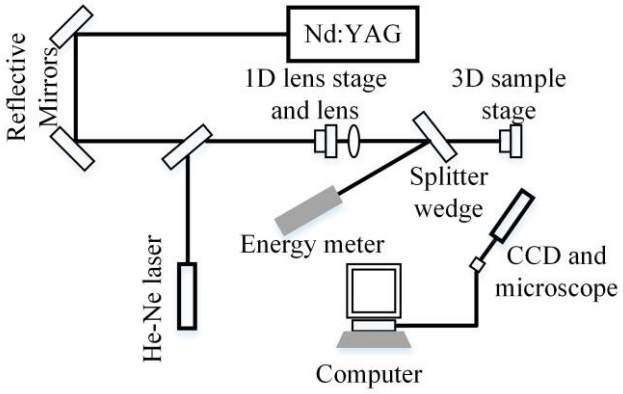

Fig. S1. Schematics of laser irradiation damage testing equipment

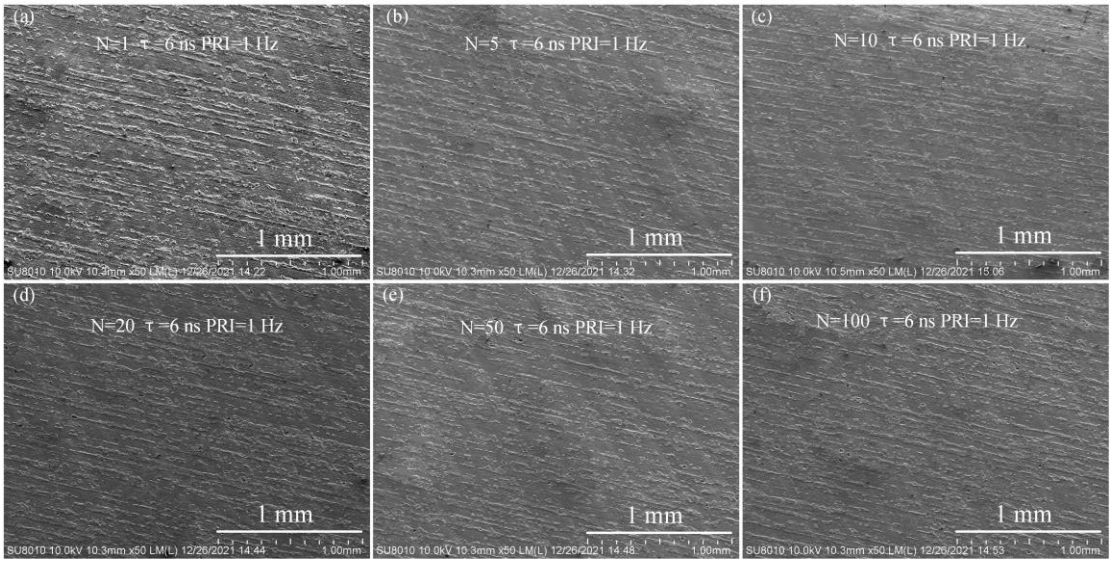

Fig. S2. 355-nm Nd:YAG laser irradiation of aluminum alloy 6061 with functional layers at a fluence of 0.5 J/cm2 at (a)1 time, (b) 5 time, (c) 10 time, (d) 20 time, (e) 50 time, (f) 100 time irradiation.